



# Damage tolerance of carbon-carbon composites in aerospace application



Piyas Chowdhury<sup>a</sup>, Huseyin Sehitoglu<sup>a,\*</sup>, Richard Rateick<sup>b</sup>

<sup>a</sup> Department of Mechanical Science and Engineering, University of Illinois at Urbana-Champaign, 1206 W. Green St., Urbana, IL 61801, USA

<sup>b</sup> Honeywell Aerospace, 3520 Westmoor St., South Bend, IN 46628, USA

## ARTICLE INFO

### Article history:

Received 21 April 2017

Received in revised form

19 September 2017

Accepted 4 October 2017

Available online 8 October 2017

## ABSTRACT

We investigate fatigue-cracking behavior of unidirectionally reinforced carbon-carbon composites with different fiber orientations aimed for aerospace applications. Through digital image correlation (DIC), full field displacements are recorded in-situ, which capture the evolution of strain localizations during cyclic loading. DIC displacement fields are further utilized to determine crack driving forces via a regression analysis of orthotropic constitutive relations. Microscopic computerized tomography (micro-CT) scans disclose the competing nature of damage micromechanism e.g. pore coalescence, fiber bridging etc. for an advancing crack. Electron microscopy of fractured surfaces reveals widespread fiber/matrix interface debonding and fiber pullout, which chiefly contribute to cyclic cracking resistance. Upon sufficient progression, cyclic crack growth is observed to be self-arresting in nature unless applied loads are further increased. The origin of such behavior is attributed to: (a) reduction of driving forces due to continually degrading composite elastic modulus and (b) enhanced damage impedance originating from resistive tractions due to pervasive fiber bridging and pullout in the wake.

© 2017 Published by Elsevier Ltd.

## 1. Background

Carbon fiber/carbon matrix (abbreviated “C/C” henceforth) composites possess a unique combination of mechanical properties, which makes them highly sought-after engineering materials in aerospace industries [1–3]. Superior thermal stability, wear resistance, heat transferability, ultra-light weight etc. constitute some of their salient attributes [4,5]. Notable examples of C/C composite application under extreme conditions include heat-shields in re-entry vehicles, nozzles in rocket motors, high friction members in aircrafts, to name a few [6]. The current C/C material (unidirectionally reinforced) in question has the designated usage as rotor/stator discs in the braking system of an aircraft landing gear (Fig. 1). Such an application is specifically susceptible to disastrous failures. Several outstanding issues can be pinpointed, namely: (i) structural deterioration due to high temperature oxidation (friction-generated) when engaging brakes and (ii) secondly, persistent fatigue cracking induced by fluctuating loads during multitudes of brake-and-release operations. Extensive laboratory investigations can provide valuable fail-safe information

about these matters, and help safeguard component life. While the former is undertaken in the most recent literature [7,8], we embark on examining the latter problem on the subject of fatigue damage tolerance. In its typical service lifetime, a C/C composite brake would invariably be subjected to detrimental fatigue loads in the course of frequent landing and taxiing of the aircraft. Given the strong microstructural dependency of composite mechanical properties, a detailed characterization of cyclic damage responses and the microstructural origin thereof would be of immense significance. Specifically, the fiber orientation sensitivity on the cycle damage resistances needs to be established given the nature of dynamic loads operative throughout the brake life. In this paper, we probe into the fatigue crack propagation behavior of selected C/C composite microstructure with an assortment of modern experimental techniques. Specifically, the crucial roles of fiber orientation, fiber/matrix interface, pore etc. are extensively characterized, and the governing micromechanisms clarified.

The microscopic origin of static fracture and fatigue in composites can be very complex to understand due to highly anisotropic and non-Hookean nature of its elastic deformation [9–11]. The anisotropy arises chiefly from the directional weaving of the fiber reinforcements, which oftentimes can deviate from perfect layout and form localized bundles. The non-linear elasticity stems

\* Corresponding author.

E-mail address: [huseyin@illinois.edu](mailto:huseyin@illinois.edu) (H. Sehitoglu).

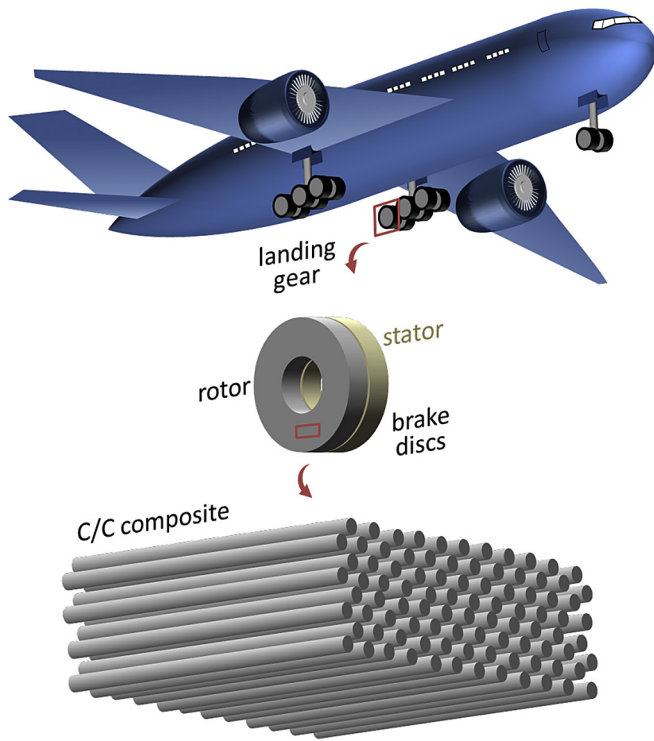


**Fig. 1.** The C/C composite material studied in the present study is used to make the brake discs (stator and rotor) of aircraft landing gears. (A colour version of this figure can be viewed online).

from low stiffness carbon matrix having slightly viscoelastic attributes, which surrounds the less compliant (i.e. with high stiffness) fibers. Due to the strong mismatch between matrix and fiber elasticity, quite unique physical processes are operative at the microscale governing the overall composite constitutive properties [12]. For instance, under applied forces the soft matrix would be vulnerable to delamination and hence cracking. The matrix crack, once it reaches the fiber/matrix interface, could either immediately break or bypass the fiber by detaching from it. If the crack front is encountered mostly with instantaneous fiber breakage, the cracking would lead to catastrophic brittle fracture with a smooth post-fracture surface morphology. By contrast, a widespread interfacial debonding would allow matrix cracking to continue while the fibers in the wake would form bridges and eventually be subjected to pulling out of the matrix sockets [13]. This situation would essentially give rise to enhanced resistive forces in the crack wake, thereby impeding crack opening and sliding displacements. In other words, superior crack growth resistance can be directly traced back to the ease of matrix/fiber detachment. One can list the factors such as interface debonding, crack deflection, fiber bridging and pullout as the principal mechanisms that synergistically contribute to cracking impedance [14]. On the other hand, intra-matrix delamination, formation and merger of micro-pores etc. assist in faster cracking. Deformation scenario would be further compounded for cyclic variation of loads, which would additionally give rise to irreversible localized phenomena upon thousands of cycles. Factors such as the nature of fiber weaving, fabrication processes, stress ratio would also modify the cyclic fracture behavior [15–17]. Given the inherently complicated micro-mechanisms of composite fracture, it is imperative to characterize the operative physical processes in details along with macroscale characterizations.

To that end, we employed extensive mechanical testing to study

both monotonic and cyclic attributes of C/C composites with two distinct unidirectional fiber layouts (detailed in next section). We note the challenges associated with precise pinpointing of the crack tip by optical microscopy alone. To overcome this technical issue, we adopted digital image correlation (DIC) [18], whereby full field displacements in an area of interest enveloping the advancing crack were tracked. This, in addition, assisted in constructing local strain contours during cyclic loading. Computerized tomography (CT) scans facilitated the understanding of three-dimensional nature of the advancing crack. This method specifically revealed the roles of pores, fiber bridging etc. on the crack propagation behavior. Then, the post-fracture crack surface morphology was studied using scanning electron microscopy (SEM) in order to uncover fiber pullout mechanism, interface debonding, crack branching etc.

## 2. Materials and methods

### 2.1. Materials

The current C/C composites consist of hard carbon fibers, the fabrication of which consists of multiple steps [6]. First, fibers of polyacrylonitrile (PAN, a semicrystalline organic polymer) were subjected to oxidation between 200 °C and 300 °C temperatures in oxygen- or ozone-enriched air. The oxidation process stabilized the polymer via enhancing fiber cross-linking, which in turn precluded fiber collapsing during the subsequent carbonization. Next, the oxidized fibers underwent carbonization performed at temperatures ranging from 1000 °C to 1500 °C in inert (nitrogen- or argon-filled) environment. As a result of carbonizing, the fibers lost 50% of the overall weight due to volatilization of other compounds (e.g. water, methane, ammonia). Upon the carbonization, the fibers became highly dense, comprising upwards of 92% by weight of carbon. Finally, the relatively softer carbon matrix was introduced into the non-woven or felt-like fabric preform by *chemical vapor infiltration (CVI)* process. The densified composite was heat-treated to increase the graphitic nature of the material. For more details on the fabrication and chemical properties of the current materials, the readers are referred to [7,8].

### 2.2. Methods

In the present research, tension and fatigue crack growth tests were performed using a servo-controlled Instron 8501 A machine and suitably-fabricated dog-bone shaped specimens. The specimen was firmly gripped between the actuators. Applied mechanical forces and/or displacements during testing were controlled through computer terminal. The experimental setup and the characterization methodologies (DIC, micro-CT scan, SEM) is schematically summarized in Fig. 2. Further details follow.

Digital image correlation (DIC) [18–20] was employed to measure in-situ full-field displacements on the specimen surface. Pre-DIC preparation of the sample involved: (a) polishing of the surface of interest to a mirror finish using abrasive paper, (b) application of dark paint using airbrush to create a speckle pattern of random (Gaussian) distribution. A digital camera (with a resolution of 1600 × 1200 pixels and at a maximum frame rate of 15 fps) was used to capture images of the speckled surface in real-time. The corresponding loads were measured by a 7.5 kN load cell attached to one of the actuators. The global strain levels (as in Figs. 4–6) were measured by taking the mean value of all strains within a DIC area of interest of size 3 mm × 6 mm (approximately). For the fatigue testing, when the crack initiated from the notch and started advancing, a greater number of images per cycle were captured at a regular interval. A commercial program (Vic2D) was used to correlate the images corresponding to the deformed surface with

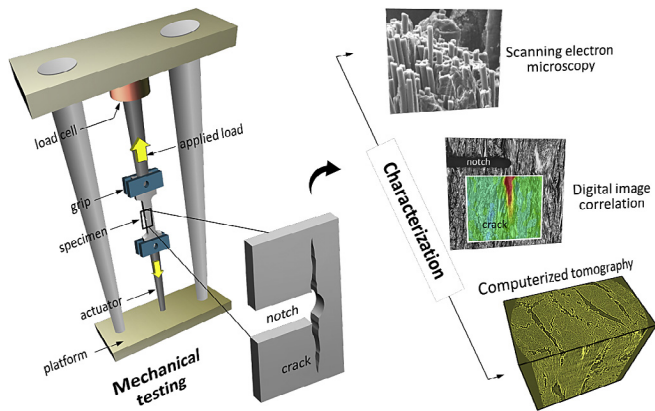


**Fig. 2.** Schematic illustration of the investigative methods undertaken in the current study. Tension and fatigue tests are conducted on dog-bone shaped specimens, and the evolution of cracking is characterized with multiple optical techniques – in-situ digital image correlation (DIC), ex-situ scanning electron microscopy (SEM) and computerized tomography (CT) scans. (A colour version of this figure can be viewed online).

the reference image (i.e. with no deformation). For fatigue, the image captured at the minimum load ( $K_{min}$ ) for a certain measurement cycle was considered the reference image. Two subsets on each crack flank (i.e. acting as “digital extensometers”) were earmarked to measure displacements in the neighborhood the advancing crack [21,22]. Multiple digital extensometers were used along the entire length of the crack (i.e. from the crack tip to its wake towards the notch). Consequently, the opening ( $u$ ) and sliding ( $v$ ) displacements and the associated strain (Lagrangian) levels were captured. The displacements were subsequently utilized in a least-squares regression algorithm to determine mode I and II stress intensity factors. The captured images were also used to obtain the advancing crack length,  $a$ , and its increment per cycle ( $da/dN$ ) in-situ in the Vic2D software. During the propagation of the crack, the regularly-captured images of the painted surfaces near the crack were compared with a reference image in the Vic2D software (in terms of displacement fields).

Scanning electron microscopy (SEM) and optical microscopy were used to analyze the microstructure of the deformed specimens. Micro computerized tomography (micro-CT) scans were performed prior to the final fracture to understand the crack growth mechanism. We utilized Xradia MicroXCT-200 at the Beckman Institute of University of Illinois [23]. This particular setup is capable of non-destructive analysis of samples by means of high-resolution 3D X-rays with sub-micron pixels. For our samples, the micro-CT scans were taken considering a cubic volume of  $1.3 \text{ mm} \times 1.3 \text{ mm} \times 1.3 \text{ mm}$  in the wake of the lower crack. The scan used a 10X magnification lens, and has a pixel size of  $2 \mu\text{m}$ . At the time when the scan was taken, the sample underwent 370,000 cycles in the fatigue cycling experiment.

Geometrical features of a typical fatigue specimen are presented in Fig. 3. The specimens were machined (to create the dog-bone geometry and the notch) using polycrystalline diamond coated tooling. The total length of the specimen was 33 mm in gage length, width and thickness being 15 mm, 3 mm and 1.2 mm respectively. The fibers were oriented unidirectionally as the schematics suggest. Although some surface bundles were discerned through optical microscopy, the bulk of the material (through thickness) was consistent in terms of fiber weaving. Considering fiber direction with respect to the applied loading direction, we classify the current specimens into two categories: vertical-fiber and horizontal-fiber composite materials. The fibers in the vertical case were parallel to the loading direction, and the longitudinal axis was

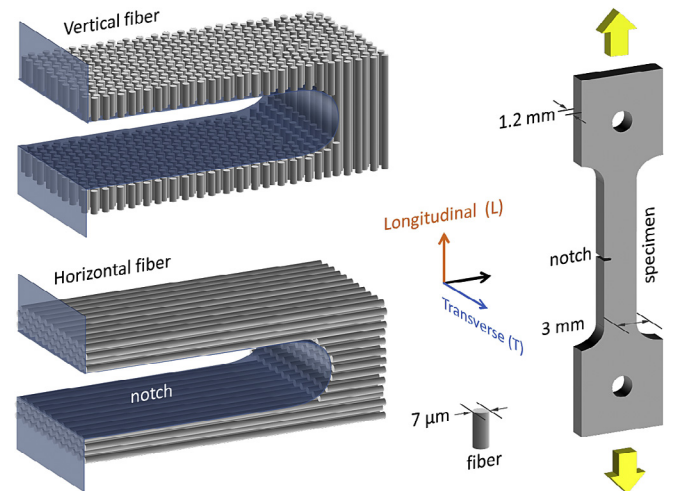


**Fig. 3.** The specimens used for fatigue crack growth tests is of dog-bone type. Two types of fiber mesh orientations are studied – horizontal and vertical. (A colour version of this figure can be viewed online).

denoted “L”. The horizontal fibers were perpendicular to the loading direction and parallel to the transverse axis denoted as “T”. A notch of size 1/2 or 1/6 of the specimen width was introduced in the middle of the gage section. The purpose of the notch was to initiate the crack in this preferred location so that during its propagation we could focus the camera onto the area of the interest. The uniaxial tension specimens were of the same geometry without any notch. A hole was introduced in each grip section to have better gripping during the tests. Fatigue crack growth experiments were conducted under load control using a triangular waveform with 3 Hz or 1 Hz cyclic frequency at a load ratio of 0.05 until a crack was initiated from the notch. The peak stress values (i.e.  $\sigma_{max}$ ) during fatigue cycling for different specimens (so as to initiate the crack and study its stable propagation) were in the range of 20 MPa–40 MPa. Once a crack had initiated, DIC images were captured for 100–500 cycles at an interval of 15000 cycles. Correlations were conducted by using a maximum subset size of  $130 \mu\text{m} \times 130 \mu\text{m}$  at a step size of  $30 \mu\text{m}$ . A number of tests using multiple specimens both at a constant stress and ramped-up stresses were conducted to establish the damage tolerance trends as reported in the following sections.

It should be noted that the results that follow in the next sections are consistently observed for multiple specimens (as many as 10 specimens for each kind of test).

### 3. Results

#### 3.1. Determination of elastic moduli from monotonic tests

We conducted multiple tension and compression tests on both vertical- and horizontal-fiber specimens to establish the elastic moduli: longitudinal modulus ( $E_L$ ), transverse modulus ( $E_T$ ). Fig. 4 presents two typical tensile stress-strain responses for the vertical- and horizontal-fiber composites. From the slopes of multiple sets of experimental data, the magnitude of the longitudinal modulus,  $E_L$ , is established to be  $40 \pm 1 \text{ GPa}$ . Similarly, by conducting numerous tests on the horizontal fiber specimens, the transverse modulus,  $E_T$ , is measured to be  $10 \pm 1 \text{ GPa}$ . In the fatigue analysis, these constants serve as crucial input for determining the crack driving force (discussed in section 3.3).

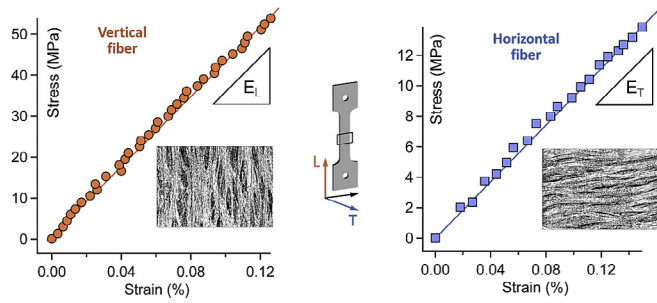


**Fig. 4.** Stress-strain responses for the composite specimens with vertically and horizontally oriented fibers. (A colour version of this figure can be viewed online).

### 3.2. DIC study of cyclically evolving strain localizations

We performed DIC analysis on two consecutive cycles of loading/unloading using un-notched specimens. In Fig. 5, we present the results on the first cycle of loading/unloading. Notice the irreversibility of stress-strain response as the fully unloaded material retains residual strain. At the end of loading, a global strain level of 0.15% gives rise to a maximum local strain of 1%. The corresponding stress level is about 14 MPa. Note that the unloading curve is characterized by a reduced magnitude of the slope (i.e. modulus). The DIC strain maps (insets) suggest that the local deformation is of highly heterogeneous nature, exhibiting multiple strain bands parallel to fibers. Upon unloading, the smaller strain bands are fully recovered. On the other hand, the larger bands of strains are retained as residue after full unloading. While the unrecoverable bands are the result of damaged fibers, matrix and merged pores, the reversible bands correspond to localized elastic stretching. Fig. 6 presents the second cycle where the previously unloaded sample is re-loaded to a higher stress-strain level (0.23% and 20 MPa respectively) before fully unloading. The prevalence of strain bands (in the inset DIC maps) is demonstrably greater than the first cycle. Upon unloading, the largest deformation band is retained as residual strain whereas the relatively small bands are completely reversible. Moreover, the modulus degradation in the unloading curve is noted. It should be noted that the DIC strain

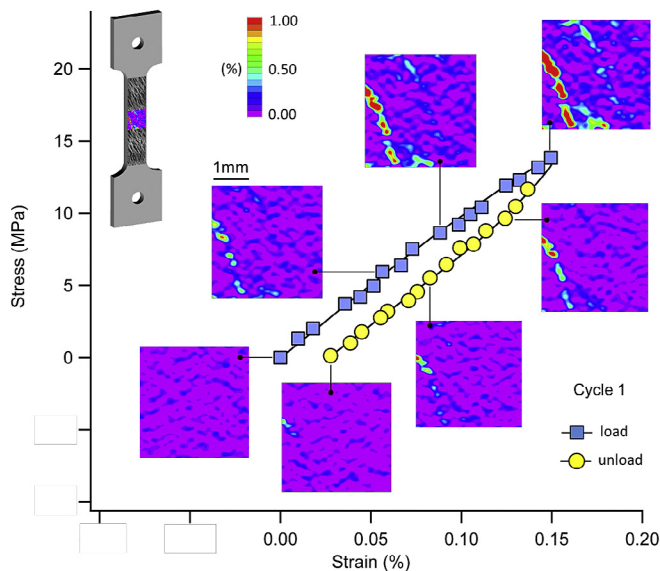


**Fig. 5.** First cycle of load/unload with local strain contours measured using DIC. (A colour version of this figure can be viewed online).

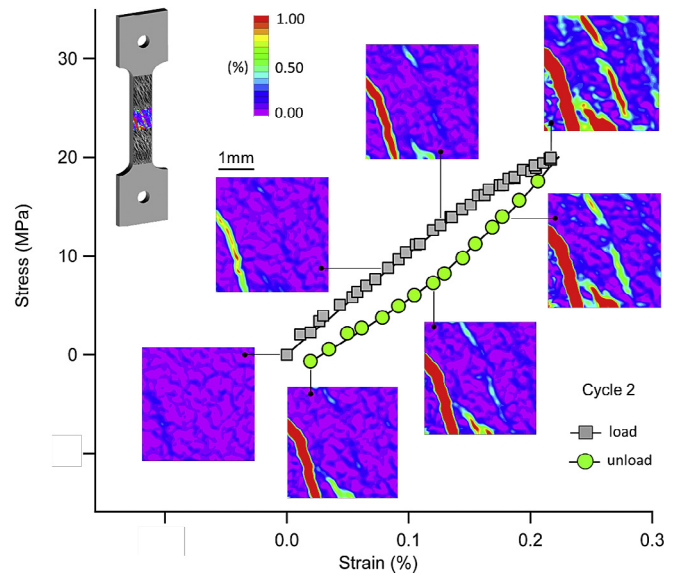


**Fig. 6.** Second cycle of loading/unloading, which demonstrates the increasingly irreversible nature of the local deformation (via DIC strain contours), which would accumulate over many cycles of fatigue. (A colour version of this figure can be viewed online).

contours inevitably contains some background noise (with strain level less than 0.002), giving rise to patch-like regions in other areas. Notwithstanding the noise, the technique is demonstrably useful in identifying the localizations of strains and better quantifying the small-scale damage evolution.

The nature of cyclic strain localizations as studied based on two consecutive cycles bear important implications regarding fatigue damage accumulation mechanism. Since a substantial degree of local strain irreversibility is evidenced upon cycling, it is reasonable to deduce that such irreversibility would potentially be accumulated over multitudes of fatigue cycles. Particularly, note that a mere stress level of 20 MPa induced considerable degree of irreversibility. The microstructure retained a residual strain bands with magnitudes reaching 1% at a global stress level as low as 14 MPa. Thus, continued cycles of load/unload, it can be inferred, would essentially give rise to accumulated and highly localized damage bands throughout the material microstructure, leading to micro-crack initiation and subsequent propagation. In addition, the overall modulus of the composite has also been observed to undergo steady decline as the cyclic loads continue. We will discuss next how the deterioration of the modulus would ultimately lead to a depreciation of the crack driving forces.

### 3.3. CT scan analysis of fatigue crack growth

For the duration of continued cyclic loading up to the final fracture of the specimen, two cracks are nucleated from the notch tip, which, hereafter, we designate as “lower” and “upper” cracks. The cracks always advance longitudinally along the fibers in both vertical- and horizontal-fiber specimens irrespective of the applied loading direction. The tests are conducted at a maximum stress level of 10 MPa (with a load ratio of 0.05). During the growth period, we perform three-dimensional CT scan of the lower crack in one of the vertical-fiber specimens as shown in Fig. 7. The crack is initiated at the tip of the notch, which then continues into the bulk. The length of the discernible crack is approximately 600  $\mu\text{m}$ . The fibers and surrounding matrix in the presence of micro-pores (near the lower notch flank) can be noticed in the 3D reconstruction of

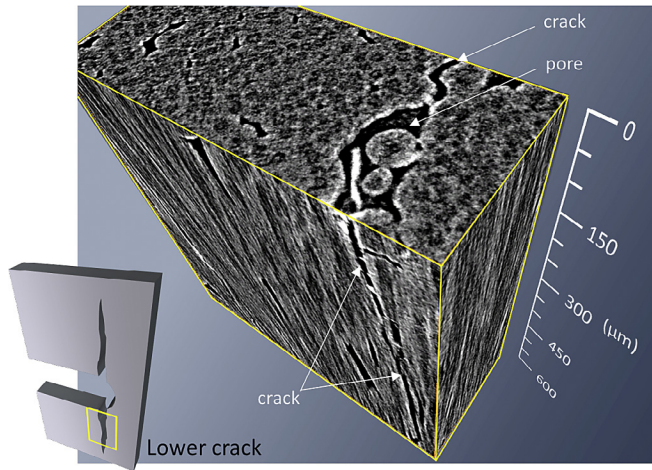


**Fig. 7.** Computerized tomography (CT) of the lower crack (in the vertical-fiber test sample), which emanates from the notch and progresses along the fiber direction. (A colour version of this figure can be viewed online).

the scanned images. Notice the presence of pores at the very base of the crack wake (i.e. close to the notch). The crack tip is situated further downwards.

In Fig. 8, scanned images at various cross-sections of the crack wake are presented. In the middle, a schematic crack is drawn to indicate the locations, where the images are taken. Note that the early cracking started at the pores. High stress concentration due to sharp curvature of the notch-tip has contributed to the initial tearing of the softer carbon matrix. Following the initiation, the crack advances via coalescence with pores in the immediate vicinity. It follows that the pores do not undergo significant enlargement as the crack intercepts them. The opening of the crack

i.e. the spacing between the crack flanks appeared substantially constricted when compared to the pore dimension. This indicates that the progressing matrix crack experiences an increasing propensity for closure. By closely inspecting different cross-sectional planes along the crack wake length, we find the evidence of fiber bridging in the wake as presented next.

In Fig. 9, four slicing planes perpendicular to the crack plane and parallel to crack growth direction are selected (designated with Roman numerals – i, ii, iii and iv). Slice i shows that the pores at the early stage of crack growth are in fact slightly elongated in geometry. Slice ii captures two pores being linked via continued tearing of the matrix as highlighted with a red rectangle. Notice that the fiber remains intact during the bridging as highlighted with a red rectangle. While slice iii shows one pore near the notch, another elongated one could be discerned further downwards (toward the crack tip).

In Fig. 10, the rectangle-highlighted region (from Fig. 9) is further elaborated, which provides a clear evidence of fiber bridging mechanism. Four closely spaced slices (marked a, b, c and d) along the crack wake show how the tearing of matrix material connects two neighboring pores. In the process, the fiber remained intact. The schematic in Fig. 10 illustrates the mechanism. A crack advancing through the matrix first merges with a pore. Under fatigue loads, the pore starts to further crack, and links with an adjacent pore. The cracking continues from this new pore until the final fracture occurs. As the crack becomes progressively longer, the extent of fiber bridging also multiplies, which ultimately contributes to crack growth resistance. We note that the phenomenon of fiber bridging indicates a relatively weak fiber/matrix interface bonding in the present C/C composites. Widespread fiber bridging eventually leads to a final failure uniquely characterized by fibers pullouts, which also provides further resistance to the composite fracture.

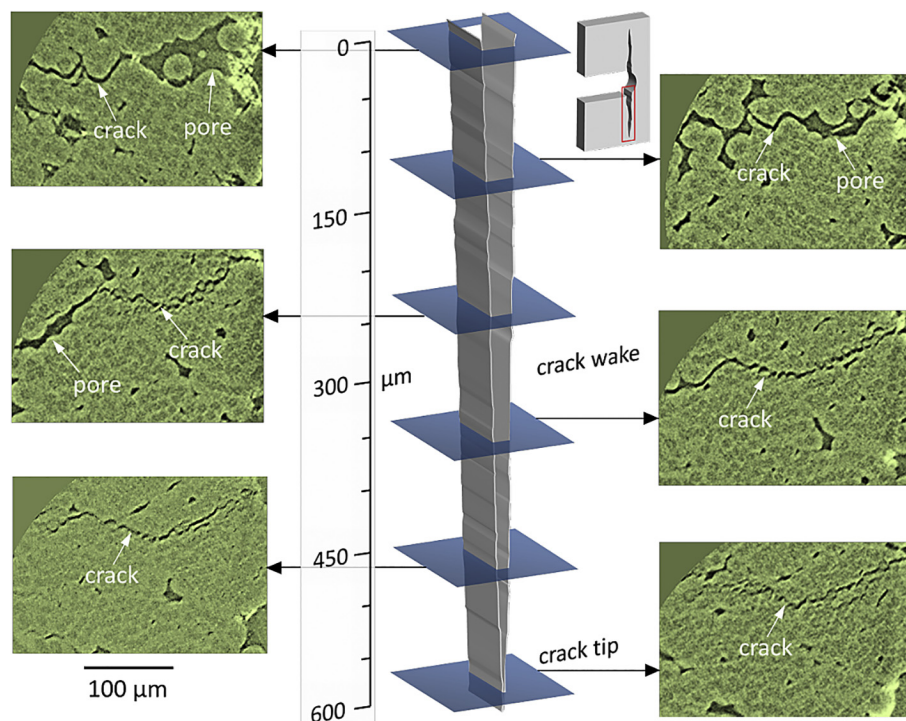


**Fig. 8.** In the vertical-fiber specimen, CT scan is performed for the lower crack at various cross-sections perpendicular to the growth direction. Notice that the initially merger of pores dictates the crack growth and subsequently tearing of matrix drives the crack advancement. (A colour version of this figure can be viewed online).

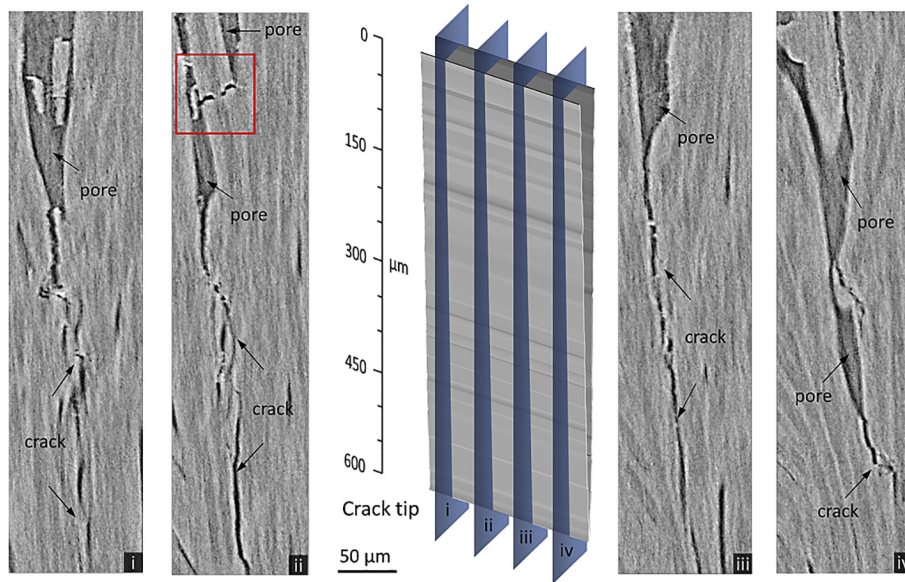


**Fig. 9.** For the specimen with vertically oriented fibers, CT scan pictures (i through iv) of the lower crack (taken at various sections parallel to the crack growth direction) shows that the crack advances by a combination of matrix tearing and merger among pores. (A colour version of this figure can be viewed online).

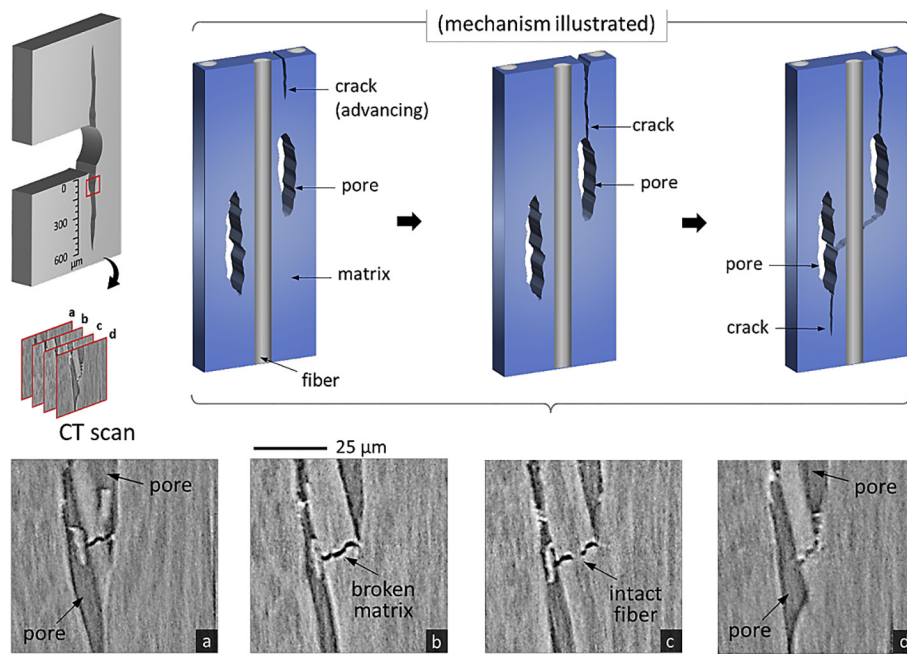
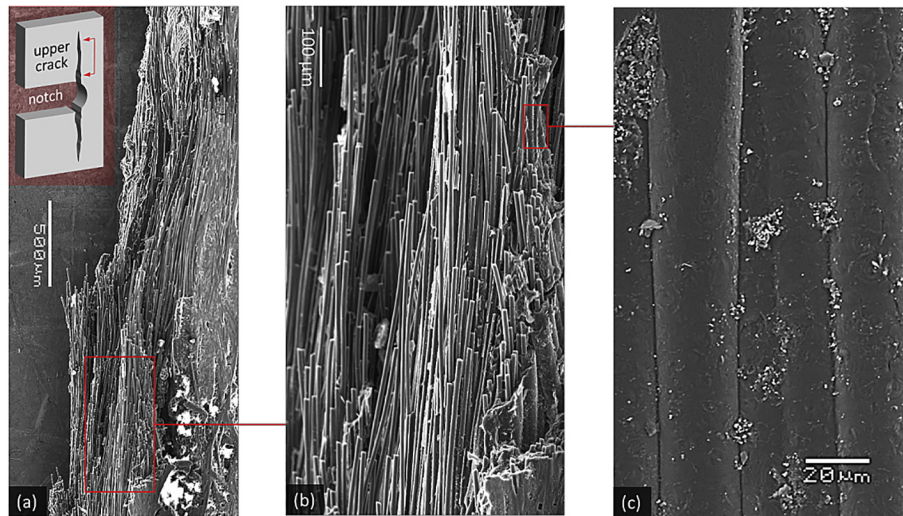


**Fig. 10.** CT scan images (a through d) at the early stage show how a growing crack coalesces with an existing pore, which then merges with a neighboring pore. The fiber remains intact (until the final fracture) while the merger of two pores advances the crack even further down. (A colour version of this figure can be viewed online).

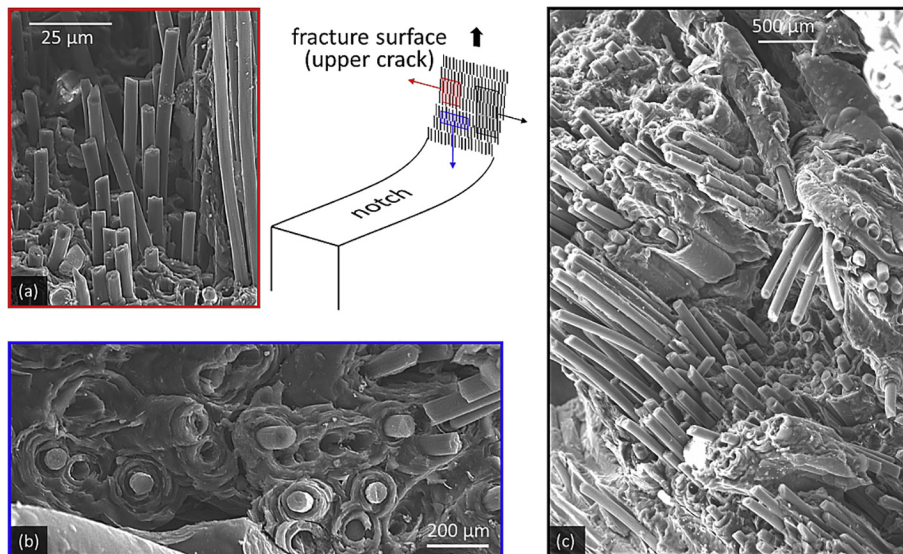
#### 3.4. SEM characterization of fracture surface morphology

Fig. 11(a) presents SEM image of the post-fracture surface of the upper crack in a vertical-fiber specimen. Final fracture occurred after the crack became progressively longer to reach beyond the static fracture toughness. From the geometry of the failure surface, the cracked surface appears to have rugged brush-like features, which, on closer inspection as in Fig. 11(b), are identified as pulled-out fibers. Fig. 11(c) show a close-up of the tightly glued fibers (note that this image is taken after polishing the fractured surface to enhance visual clarity).

Additional SEM images are taken at different locations on the fractured face of the upper crack as presented in Fig. 12(a) through (b). The pulled-out fibers are clearly visible in Fig. 12(a). A top view of another region presented in Fig. 12(b). The carbon matrix in the current composites consists of rough laminar graphitic carbon, which is circumferentially stacked around individual fibers. Also, in the literature, Bourrat noted that the basal planes of the turbostratic CVI carbon demonstrate a high degree of tangential symmetry about the fiber core [24]. The fiber cross-section is of circular geometry. From the fractographic evidence, it can be inferred that the most of the sub-critical crack growth period is characterized by



**Fig. 11.** (a) SEM image showing the face of a vertically advancing crack from the notch. (b) and (c) closer inspection of the fibers on the crack flank. (A colour version of this figure can be viewed online).



**Fig. 12.** SEM pictures (a through c) show how the fibers on the crack flank are pulled out of the softer matrix during the crack propagation. (A colour version of this figure can be viewed online).

fiber bridging and fiber withdrawal from the weaker matrix sockets.

After fracture, the de-laminated fiber-matrix interface appeared as small craters surrounded by lamellar matrix. These features are evidenced throughout the fracture surface as another example is provided in Fig. 12(c). A close-up view of the pre-fracture (polished) cross-section [7] suggests that the carbon matrix surrounding the fibers consisted of rough lamellar graphitic structure (Fig. 13). On the other hand, the post-fracture surface reveals that the matrix underwent substantial delamination during the fatigue loading. This eventually led to the fiber/matrix interface debonding. All these SEM images confirm that the failure occurred in the presence of prevalent fiber bridging and pullout. In summary, the crack growth occurred by means of tearing of soft matrix, which resulting in the fibers being debonded and pulled out of the embedding matrix.

For the horizontal-fiber specimens, however, the bridging of

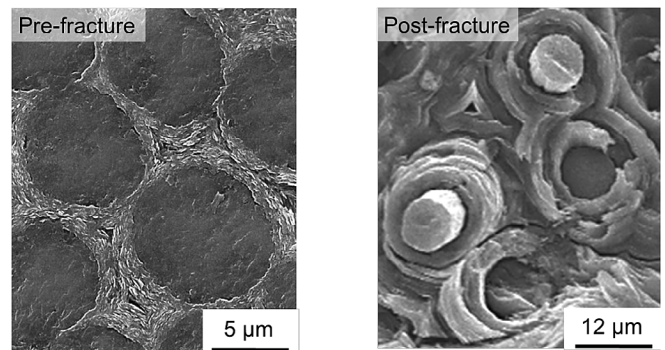


**Fig. 13.** (Left) A pre-fracture SEM close-up of a polished cross-section indicates the lamellar nature of the carbon matrix surrounding the fibers [7]. (Right) the post-fracture surface (unpolished) provides evidence of significant fatigue-induced delamination of the matrix, which ultimately led to matrix-fiber de-bonding.

fibers in the wake of the advancing crack has been observed to be in greater degree. SEM pictures in Fig. 14 show the presence of intact fibers in the very close vicinity of the crack flank. The crack path (as it appears on the surface) is highlighted with a drawn line. Notice the crack is advancing by means of matrix cracking with the fibers remaining unbroken. This is due to the fact that the applied far-field loads are acting perpendicular to the matrix-fiber interface resulting in a rapid debonding. In other words, the crack is primarily advancing due to the detachment of matrix from fibers while fibers remaining intact. This results in an increased closing traction on the crack faces, leading ultimately to enhanced crack resistance. Notice that no evidence of fiber pullout (or breaking) for the observed area of interest.

### 3.5. DIC analysis of near-crack strain fields

It is important to establish the roles of normal and shear strains on driving the crack. With DIC, we determine the strain fields responsible for mode I and mode II crack growths as presented in Fig. 15 (for a vertical-fiber specimen). Two vertical cracks (parallel to fibers as well as to the applied loads) are displayed schematically whereupon  $\epsilon_{xx}$  and  $\epsilon_{xy}$  strain contours (pertaining to crack opening and sliding respectively) are superimposed. Notice that the  $\epsilon_{xx}$  component (i.e. normal strain on the crack flanks) is more dominant than the shear strain despite the far-field loads being parallel to the crack. This is a result of the strong anisotropic nature of the C/C composite microstructure. From such analyses, it is evident that the interfacial debonding (between the fiber and the matrix) occurs due to tensile forces on the crack flanks. This effect would be even more pronounced for the horizontally oriented fibers (not shown). The degree of tensile forces on the crack flank would be considerably greater since the applied load is now perpendicular to the crack growth direction. In other words, the horizontal fiber specimens would undergo relatively easy fiber/matrix debonding due to stronger normal forces, which in turn would promote a greater extent of fiber bridging and then fiber pullout. As we will show

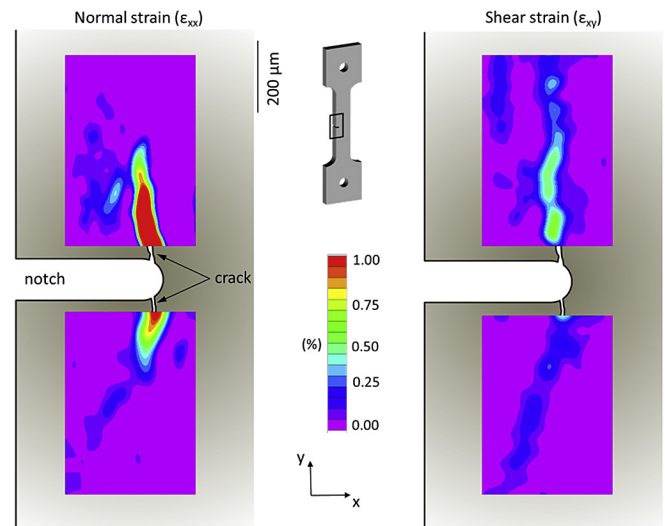


Fig. 15. Mode I and mode II strain contours ( $\epsilon_{xx}$  and  $\epsilon_{xy}$  respectively) around the upper and lower cracks as measured from the digital image correlation (DIC). (A colour version of this figure can be viewed online).

next, the horizontal fiber specimens consequently demonstrate a higher resistance to crack growth.

### 3.6. Determination of crack driving forces via regression analysis

We utilize the full field displacements measured from DIC as input to determine mode I and mode II stress intensity factors ( $K_I$  and  $K_{II}$  respectively), which are then used to calculate corresponding energy release rates ( $J_I$  and  $J_{II}$ ). DIC measurements are recorded in-situ to capture the strains on the specimen surface during an instant of fatigue crack growth. The generic constitutive relations among the crack tip displacements  $u$  (sliding),  $v$

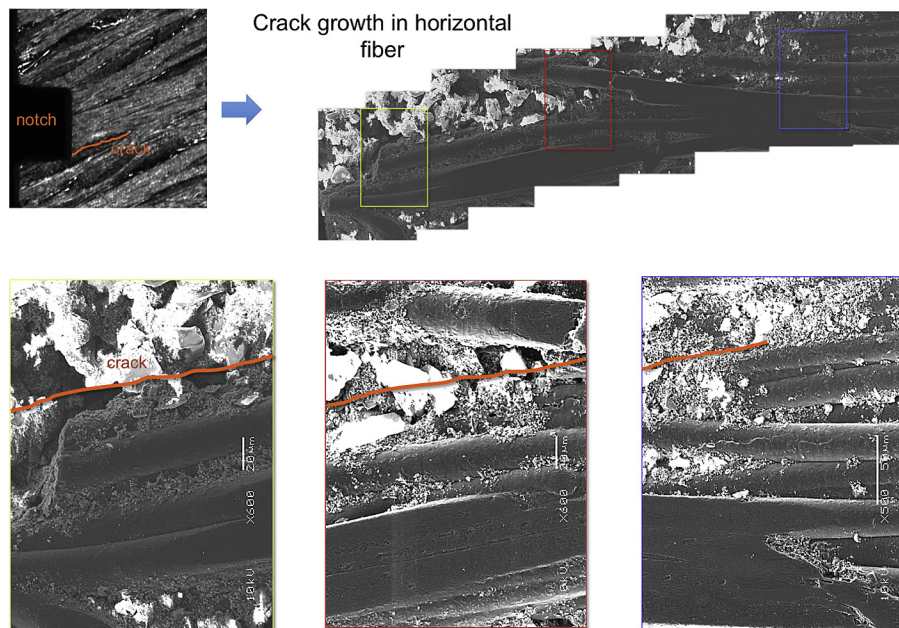


Fig. 14. SEM images showing cracking of one of horizontal-fiber specimen (as it appears on the surface). Notice that the fibers in the immediate vicinity of the crack flank are intact. (A colour version of this figure can be viewed online).

(opening),  $K_I$  and  $K_{II}$  for an orthotropic material are well established in the literature [25,26], and expressed in Equations (1) and (2).

$$u = K_I \sqrt{\frac{2r}{\pi}} \operatorname{Re} \left[ \frac{1}{\mu_1 - \mu_2} \left( \mu_1 P_2 \sqrt{\cos\theta + \mu_2 \sin\theta} - P_1 \sqrt{\cos\theta + \mu_1 \sin\theta} \right) \right] + K_{II} \sqrt{\frac{2r}{\pi}} \operatorname{Re} \frac{1}{\mu_1 - \mu_2} \left[ \left( P_2 \sqrt{\cos\theta + \mu_2 \sin\theta} - P_1 \sqrt{\cos\theta + \mu_1 \sin\theta} \right) \right] + a_{11} T r \cos\theta - A \sin\theta + B_u \quad (1)$$

$$v = K_I \sqrt{\frac{2r}{\pi}} \operatorname{Re} \left[ \frac{1}{\mu_1 - \mu_2} \left( \mu_1 q_2 \sqrt{\cos\theta + \mu_2 \sin\theta} - \mu_2 q_1 \sqrt{\cos\theta + \mu_1 \sin\theta} \right) \right] + K_{II} \sqrt{\frac{2r}{\pi}} \operatorname{Re} \frac{1}{\mu_1 - \mu_2} \left[ \left( q_2 \sqrt{\cos\theta + \mu_2 \sin\theta} - q_1 \sqrt{\cos\theta + \mu_1 \sin\theta} \right) \right] + a_{12} T r \sin\theta + A \cos\theta + B_v \quad (2)$$

where  $\operatorname{Re}$  indicates the real part of a complex number;  $K_I$  and  $K_{II}$  are the mode I and mode II stress intensity factors;  $T$  denotes the T-stress, which is the uniform stress component parallel to the crack;  $A$  stands for the rigid body rotation;  $B_u$  and  $B_v$  are the rigid body translations in the  $u$  and  $v$  directions;  $r$  and  $\theta$  are the polar coordinates with the origin at the crack tip;  $\mu_1$  and  $\mu_2$  are the two complex conjugate roots with positive imaginary parts from Equation (3) where  $a_{ij}$  are the compliance constants in the crack tip coordinate frame;  $p_i$  and  $q_i$  ( $i = 1, 2$ ) are obtained from Equations (4) and (5) respectively.

$$a_{11}\mu^4 - 2a_{16}\mu^3 + (2a_{12} + a_{66})\mu^2 - 2a_{26}\mu + a_{22} = 0 \quad (3)$$

$$P_i = a_{11}\mu_i^2 + a_{12} - a_{16}\mu_i \quad (4)$$

$$q_i = a_{12}\mu_i + \frac{a_{22}}{\mu_i} - a_{26} \quad (5)$$

For anisotropic material, the compliance constants  $a_{ij}$  are determined as follows:  $a_{11} = \frac{1}{E_T}$ ,  $a_{12} = -\frac{0.5}{E_T}$ ,  $a_{16} = 0$ ,  $a_{66} = \frac{1}{G_{LT}}$ ,  $G_{LT} = 6 \text{ GPa}$  (obtained from Ref. [27]),  $a_{22} = \frac{1}{E_T}$  and  $a_{26} = 0$ . In Equations (1) and (2), the unknown variables are  $K_I$ ,  $K_{II}$ ,  $A$ ,  $T$ ,  $B_u$  and  $B_v$ . From DIC, two distinct sets of experimental data are obtained: (a) vertical displacements,  $v$  responsible for crack opening (i.e. giving rise to mode I growth) and (b) sliding displacements,  $u$  corresponding to crack flank shearing (i.e. accounting for mode II growth). Based on a non-linear least-square regression scheme, several thousand data-points were used to generate near-crack displacement fields. Thus-constructed displacement contours for upper and lower cracks are presented in Fig. 16, as examples. The blue curves represent the DIC-measured opening and sliding displacements both for upper and lower cracks. With this information at hand, the solutions of  $K_I$  and  $K_{II}$  are sought such that the analytical displacement fields from regression (dotted red curves) are in reasonable agreement with the experimental ones (solid blue curves). It is worth mentioning here that when the crack propagates under cyclic loads, the moduli of the C/C composites (i.e.  $E_L$ ,  $E_T$  and  $G_{LT}$ ) are reduced as evidenced in the earlier load-unload experiments. Therefore, we adopt a linear scheme of modulus degradation in the above regression analysis. The magnitudes are reduced to 90% after a considerable number of load reversal cycles are executed.

### 3.7. Crack driving force versus growth rate correlation

We utilize the concept of energy release rate differential ( $\Delta J$ ) to denote the fatigue crack-driving force for the present C/C composite problem. From Equations (6) and (7) [26], we evaluate the corresponding levels of  $J_I$  and  $J_{II}$  using the already-determined  $K_I$  and  $K_{II}$  values.

$$J_I = \pi K_I^2 \sqrt{\frac{a_{11} a_{22}}{2}} \left[ \sqrt{\frac{a_{22}}{a_{11}}} + \frac{2a_{12} + a_{66}}{2a_{11}} \right]^{1/2} \quad (6)$$

$$J_{II} = \pi K_{II}^2 \frac{a_{11}}{\sqrt{2}} \left[ \sqrt{\frac{a_{22}}{a_{11}}} + \frac{2a_{12} + a_{66}}{2a_{11}} \right]^{1/2} \quad (7)$$

For an orthotropic material with the crack on one plane of symmetry, the mode I and II are independent of each other. Thus, the energy release rate differentials (between the beginning and

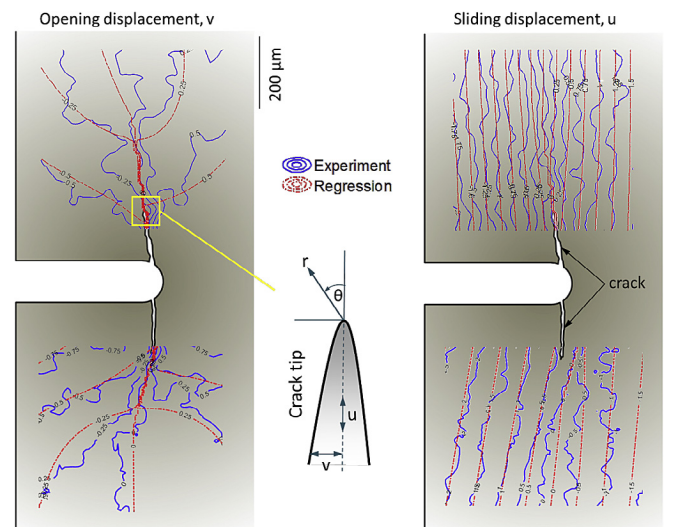


**Fig. 16.** Opening (mode I) and sliding (mode II) displacement-fields in the neighborhood of lower and upper cracks measured from DIC (blue) as superimposed with analytically determined ones (via regression algorithm). (A colour version of this figure can be viewed online).

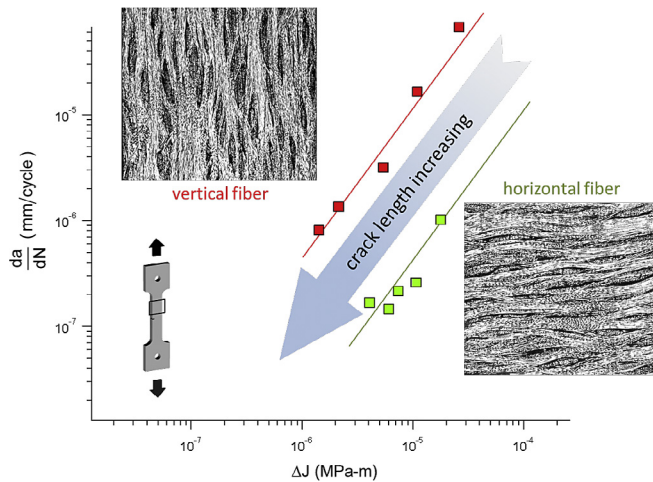


**Fig. 17.** Fatigue crack growth rate ( $da/dN$ ) versus the energy release rate differential ( $\Delta J$ ) of horizontal- and vertical-fiber composites (yellow lines indicating the crack profiles as they appear on the surface). With the progression of the crack (since its initiation), it undergoes gradual deceleration as the schematic arrow implies. (A colour version of this figure can be viewed online).

the end of a fatigue cycle) for two modes can be obtained from simple linear superposition i.e.  $\Delta J = \Delta J_I + \Delta J_{II}$ . Next, the crack growth rate,  $da/dN$ , is obtained by measuring the crack extension between two consecutive cycles at a certain instant of crack growth via finite difference method.

Thus-obtained  $da/dN$  versus  $\Delta J$  trends for vertical- and horizontal-fiber C/C materials are presented in Fig. 17. Most notable observations are as follows:

- The fatigue crack growth resistance is greater when the fibers are perpendicular to the applied loading direction (i.e. for the so-called “horizontal fiber” specimens). This is manifested in the form of these specimens demonstrating substantially reduced  $da/dN$ . It is important to note that the actual difference between the vertical- and horizontal-fiber samples is manifested in the degree of fiber bridging. From a microscopic standpoint, the mechanism is essentially similar for both cases, in that the softer matrix is continually damaged followed by fiber bridging in either situation. Due to different orientations for horizontal and vertical fibers (i.e. with respect to the global loads), it is the extent and the speed of matrix tearing and fiber bridging, which in fact differ mechanistically. In other words, it would be judicious to interpret the mechanistic difference of crack growth processes for two fiber orientations in terms of increased or decreased amount of tearing/bridging phenomena.
- Cracks in either fiber orientation are found to be self-arresting in nature. At the early stage, the growth rate of the small crack is high. As the crack becomes progressively longer, it decelerates significantly, and comes to an arrest unless the applied far-field stress is increased.

## 4. Discussion

### 4.1. Damage accumulation

In other conventional engineering materials (e.g. metallic [28,29], polymeric [30]), the role of interface-induced weakening during crack propagation is well-known. The interfaces in composite materials, however, are quite special, in that the fibers typically possess high strength and modulus while the matrix, being the binding material, is relatively weak. A strongly-bound

fiber/matrix interface would cause a simultaneous breakage of matrix and fiber to satisfy compatibility [13]. On the other hand, in case of weak interfacial bonding, the matrix would first separate from fibers, and continue to break without causing significant damage to the fibers [31]. In early literature, an overall toughening of C/C composites was noted as a direct consequence of such detachment [32,33]. The phenomenon is a result of the ability of softer matrix to undergo large deformation. This also gives rise to the formation of widespread isolated microscopic pores in addition to the primary crack. In the present materials, the cyclic damage occurs via highly localized yet incremental strain accumulation. From the DIC strain maps, we observe that small yet irreversible strain bands are formed during cyclic loading aligned with the fibers. Consequently, the overall modulus undergoes gradual degradation. The lamellar morphology of the carbon matrix makes them particularly susceptible to delamination. The relative ease of debonding of the matrix can be attributed to its rough laminar structure, which is a function of fabrication variables [34,35].

### 4.2. Deceleration of crack growth

Earlier, Sakai and co-workers [13,36,37] conducted extensive studies on static fracture of C/C composites, and concluded that the matrix cracking is first to initiate from possible sources such as pre-existent defects (e.g. pores) with high stress concentration [38]. This is followed by fiber bridging and then by fiber pullout in the crack wake. As the crack becomes progressively longer, the tractions generated due to collective fiber bridging would be further enhanced, thereby effectively decelerating the crack growth. Likewise, as the wake of the crack grows larger, sites of fiber pullout would be greater in number. The fiber bridges decelerate the crack growth by resisting the crack opening. The pullout of fibers from the matrix socket requires overcoming friction at the interface. The combined retarding effects of fiber bridging and fiber withdrawal would necessitate application of additional forces in order for the crack to advance. Consequently, the ever-building resistance towards further cracking would cause a stage of self-arrest [9]. Therefore, the ultimate fracture would occur when the applied far-field stress is amplified to the effect of re-driving the crack to catastrophic failure.

We noted that with increasing crack length both the driving force ( $\Delta J$ ) and the growth rate ( $da/dN$ ) is consistently reduced. Moreover, when the applied farfield forces are perpendicular to fibers (i.e. in horizontal-fiber specimens), the crack growth resistance is even greater i.e. exhibiting a reduced degree of  $da/dN$ . The

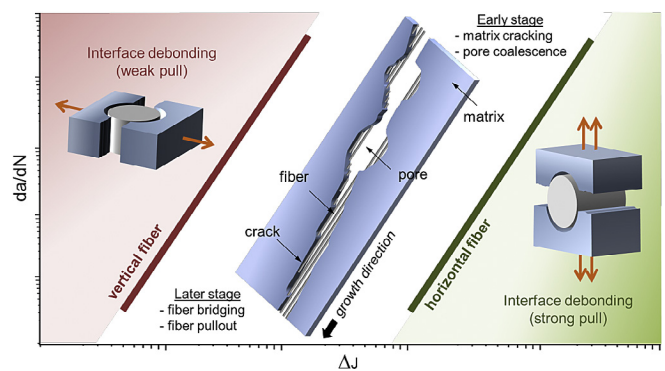


**Fig. 18.** Schematic elucidation of  $da/dN$  trends for vertical and horizontal fiber composites (i.e. parallel and perpendicular to applied loads respectively). Greater interface debonding promotes enhanced fiber bridging followed by pullout, which is why horizontal fibers (under stronger pull leading to easier debonding) demonstrate reduced  $da/dN$ . (A colour version of this figure can be viewed online).

reason behind such a response is clarified in Fig. 18. The middle schematic illustrates the early and later stages of crack propagation common to both vertical- and horizontal fibers. It is worth recalling here that for either case the crack is always found to advance along the fibers lengthwise. For both fiber orientations, in the early crack advancement period, the dominant mechanisms are matrix cracking and pore coalescence. Since the wake of the incipient small crack is relatively small in length, the degree of fiber bridging and pullout events is insignificant. Consequently, the crack growth rate is fairly high. With enlarging wake regions, the fiber bridging and pullout becomes predominant in the later stage of the crack growth. Significant portion of the applied forces would be spent to overcome the pullout-induced friction as well as the bridging tractions. Consequently, the effective driving force for crack growth is reduced, therefore decelerating the growing crack.

#### 4.3. Role of interface weakening

In Fig. 18, the schematics next to the respective curves indicate the greater tensile forces (pull) are at play for interface debonding in horizontal fibers while weak tension is operative for the vertical cases. In the post-fracture SEM images, we note a considerable presence of fiber pullout, which implies to a weakening of the fiber/matrix interface during crack propagation. The damage is predominated by a widespread detachment of fibers and matrix. Moreover, the CT scan results indicate that the breakage of matrix continued immediately damaging the fibers by coalescing with diffuse microscopic pores at the early stage. From the DIC strain contours around the cracks (Fig. 15), it is evident that the development of normal strain (crack opening) is predominant while the shear component (crack sliding) is relatively weak. This trend is observed in specimens with both types of fiber orientations (note that only vertical case is presented here). We conclude that the dominance of the mode I strains on the crack flanks would result in pervasive debonding of fiber/matrix interface. In particular, for the horizontal-fiber specimens, the fiber/matrix interface debonding is expected to be greater in extent as the applied farfield loads are perpendicular to the fibers. Since the increased interface debonding means enhanced possibility of fiber bridging and pullout, the fatigue crack growth resistance for the horizontal-fiber case is higher than that of the vertical specimens.

## 5. Conclusion

In this work, we have investigated the damage tolerance behavior of unidirectionally reinforced C/C composites using various experimental techniques. The major findings can be summarized as follows.

- (1) From DIC analyses, it is observed that the accumulation of irreversible cyclic damage occurs in the form of localized strain bands parallel to fibers. These highly concentrated deformed sites serve to reduce the overall stiffness of the composite over multitudes of cycles.
- (2) During cracking, debonding of fiber/matrix interface causes pervasive fiber bridging occurs, which plays a major role in decelerating the crack growth as confirmed via CT scan analysis. In addition, from studying the post-fracture crack surfaces, an extensive fiber pullout-dominated damage progression is evidenced.
- (3) From  $da/dN$  versus  $\Delta J$  analyses, cracking under fatigue loading is found to be self-arresting in nature. Initially, the crack advances via the tearing of the matrix assisted by coalescence with pre-existent microscopic pores. In the later stage, gradually increasing extent of fiber bridging and

pullout contributes to the suppression the crack growth. Consequently, as the crack becomes progressively longer, a consistent reduction in the  $da/dN$  level is noticed. The reduction in the crack driving forces is attributed to the modulus degradation over cycles.

- (4) When the fibers are perpendicular to the applied loads, a greater degree of fiber/matrix interface debonding occurs, resulting in an enhanced bridging and pullout phenomena. This leads to superior resistance to the cyclic damage propagation.

## Acknowledgements

We are grateful to Honeywell Aerospace for sponsoring this research, and for providing the C/C composite specimens. We also thank Mr. George Li at University of Illinois at Urbana-Champaign for his contributions in the tests.

## References

- [1] J.D. Buckley, D.D. Edie, *Carbon-carbon Materials and Composites*, William Andrew, 1993.
- [2] E. Fitzer, The future of carbon-carbon composites, *Carbon* 25 (2) (1987) 163–190.
- [3] C. Soutis, Carbon fiber reinforced plastics in aircraft construction, *Mater. Sci. Eng. A* 412 (1) (2005) 171–176.
- [4] P. Morgan, *Carbon Fibers and Their Composites*, CRC press, 2005.
- [5] J. Sheehan, K. Buesking, B. Sullivan, Carbon-carbon composites, *Annu. Rev. Mater. Sci.* 24 (1) (1994) 19–44.
- [6] G. Savage, *Carbon-carbon Composites*, Springer Science & Business Media, 2012.
- [7] C. Zhang, M. Chen, S.C. Paulson, R.G. Rateick, V.I. Birss, New insights into the early stages of thermal oxidation of carbon/carbon composites using electrochemical methods, *Carbon* 108 (2016) 178–189.
- [8] Y.-C. Lin, E.M. Ruiz, R.G. Rateick, P.J. McGinn, A.S. Mukasyan, One-step synthesis of a multi-functional anti-oxidation protective layer on the surface of carbon/carbon composites, *Carbon* 50 (2) (2012) 557–565.
- [9] T. Miyajima, M. Sakai, Fiber bridging of a carbon fiber-reinforced carbon matrix lamina composite, *J. Mater. Res.* 6 (03) (1991) 539–547.
- [10] K.R. Turner, J.S. Speck, A.G. Evans, Mechanisms of deformation and failure in carbon-matrix composites subject to tensile and shear loading, *J. Am. Ceram. Soc.* 78 (7) (1995) 1841–1848.
- [11] Y. Tanabe, T. Yoshimura, T. Watanabe, T. Hiraoka, Y. Ogita, E. Yasuda, Fatigue of C/C composites in bending and in shear modes, *Carbon* 42 (8) (2004) 1665–1670.
- [12] F.E. Heredia, S.M. Spearing, A.G. Evans, P. Mosher, W.A. Curtin, Mechanical properties of continuous-fiber-reinforced carbon matrix composites and relationships to constituent properties, *J. Am. Ceram. Soc.* 75 (11) (1992) 3017–3025.
- [13] M. Sakai, R. Matsuyama, T. Miyajima, The pull-out and failure of a fiber bundle in a carbon fiber reinforced carbon matrix composite, *Carbon* 38 (15) (2000) 2123–2131.
- [14] T. Suzuki, T. Miyajima, M. Sakai, The role of the fiber/matrix interface in the first matrix cracking of fiber-reinforced brittle-matrix composites, *Compos. Sci. Technol.* 51 (2) (1994) 283–289.
- [15] A. Murdani, C. Makabe, M. Fujikawa, Fatigue and fracture behavior in notched specimens of C/C composite with fine-woven carbon fiber laminates, *Carbon* 47 (14) (2009) 3355–3364.
- [16] H. Mahfuz, M. Maniruzzaman, J. Krishnagopalan, A. Haque, M. Ismail, S. Jeelani, Effects of stress ratio on fatigue life of carbon-carbon composites, *Theor. Appl. Fract. Mech.* 24 (1) (1995) 21–31.
- [17] O. Siron, J. Lamon, Damage and failure mechanisms of a3-directional carbon/carbon composite under uniaxial tensile and shear loads, *Acta Mater.* 46 (18) (1998) 6631–6643.
- [18] J. Carroll, C. Efstathiou, J. Lambros, H. Sehitoglu, B. Hauber, S. Spottswood, R. Chona, Investigation of fatigue crack closure using multiscale image correlation experiments, *Eng. Fract. Mech.* 76 (15) (2009) 2384–2398.
- [19] M. Sutton, W. Wolters, W. Peters, W. Ranson, S. McNeill, Determination of displacements using an improved digital correlation method, *Image Vis. Comput.* 1 (3) (1983) 133–139.
- [20] M.A. Sutton, J.J. Orteu, H. Schreier, *Image Correlation for Shape, Motion and Deformation Measurements: Basic Concepts, Theory and Applications*, Springer Science & Business Media, 2009.
- [21] W. Riddell, R. Piascik, M. Sutton, W. Zhao, S. McNeill, J. Helm, Determining Fatigue Crack Opening Loads from Near-crack-tip Displacement Measurements, *Advances in Fatigue Crack Closure Measurement and Analysis: Second Volume*, ASTM International, 1999.
- [22] M.A. Sutton, W. Zhao, S.R. McNeill, J.D. Helm, R.S. Piascik, W.T. Riddell, *Local Crack Closure Measurements: Development of a Measurement System Using*

- Computer Vision and a Far-field Microscope, *Advances in Fatigue Crack Closure Measurement and Analysis: Second Volume*, ASTM International, 1999.
- [23] [https://itg.beckman.illinois.edu/microscopy\\_suite/equipment/micro\\_ct/](https://itg.beckman.illinois.edu/microscopy_suite/equipment/micro_ct/).
- [24] X. Bourrat, B. Trouvat, G. Limousin, G. Vignoles, F. Doux, Pyrocarbon anisotropy as measured by electron diffraction and polarized light, *J. Mater. Res.* 15 (01) (2000) 92–101.
- [25] P. Shah, C. Tan, X. Wang, T-stress solutions for two-dimensional crack problems in anisotropic elasticity using the boundary element method, *Fatig. Fract. Eng. Mater. Struct.* 29 (5) (2006) 343–356.
- [26] G.C. Sih, P. Paris, G. Irwin, On cracks in rectilinearly anisotropic bodies, *Int. J. Fract. Mech.* 1 (3) (1965) 189–203.
- [27] L.R. Bradley, C.R. Bowen, B. McEnaney, D.C. Johnson, Shear properties of a carbon/carbon composite with non-woven felt and continuous fibre reinforcement layers, *Carbon* 45 (11) (2007) 2178–2187.
- [28] P. Chowdhury, H. Sehitoglu, R. Rateick, Recent advances in modeling fatigue cracks at microscale in the presence of high density coherent twin interfaces, *Curr. Opin. Solid State Mater. Sci.* 20 (3) (2016) 140–150.
- [29] P. Chowdhury, H. Sehitoglu, Mechanisms of fatigue crack growth—a critical digest of theoretical developments, *Fatig. Fract. Eng. Mater. Struct.* 39 (6) (2016) 652–674.
- [30] M. Alam, J.P. Parmigiani, J.J. Kruzic, An experimental assessment of methods to predict crack deflection at an interface, *Eng. Fract. Mech.* 181 (2017) 116–129.
- [31] W. Kowbel, C. Shan, The mechanism of fiber—matrix interactions in carbon—carbon composites, *Carbon* 28 (2) (1990) 287–299.
- [32] K. Goto, H. Hatta, D. Katsu, T. Machida, Tensile fatigue of a laminated carbon—carbon composite at room temperature, *Carbon* 41 (6) (2003) 1249–1255.
- [33] L. Manocha, O. Bahl, Y. Singh, Mechanical behaviour of carbon-carbon composites made with surface treated carbon fibers, *Carbon* 27 (3) (1989) 381–387.
- [34] R.E. Franklin, Crystallite growth in graphitizing and non-graphitizing carbons, *Proc. R. Soc. Lond. A Math. Phys. Eng. Sci. R. Soc.* (1951) 196–218.
- [35] J. Neumeister, S. Jansson, F. Leckie, The effect of fiber architecture on the mechanical properties of carbon/carbon fiber composites, *Acta Mater.* 44 (2) (1996) 573–585.
- [36] M. Sakai, T. Miyajima, M. Inagaki, Fracture toughness and fiber bridging of carbon fiber reinforced carbon composites, *Compos. Sci. Technol.* 40 (3) (1991) 231–250.
- [37] M. Sakai, Fracture mechanics and mechanisms of fiber-reinforced brittle matrix composites, *Nippon Seramikkusu Kyokai Gakujutsu Ronbunshi* 99 (10) (1991) 983–992.
- [38] Y. Kogo, H. Hatta, H. Kawada, T. Machida, Effect of stress concentration on tensile fracture behavior of carbon-carbon composites, *J. Compos. Mater.* 32 (13) (1998) 1273–1294.